

Spatial behavior in a Mott insulator near the voltage driven resistive transition

Arijit Dutta and Pinaki Majumdar

Harish-Chandra Research Institute, HBNI, Chhatnag Road, Jhansi, Allahabad 211019, India

(Dated: June 25, 2020)

We develop a real space theory of the voltage bias driven transition from a Mott insulator to a correlated metal. Within our Keldysh mean field approach the problem reduces to a self-consistency scheme for the charge and spin profiles in this open system. We solve this problem for a two dimensional antiferromagnetic Mott insulator at zero temperature. The charge and spin magnitude is uniform over the system at zero bias, but a bias V leads to spatial modulation over a lengthscale $\xi(V)$ near the edges. $\xi(V)$ grows rapidly and becomes comparable to system size as V increases towards a threshold scale V_c . The linear response conductance of the insulator is zero with the current being exponentially small for $V \ll V_c$. The current increases rapidly as $V \rightarrow V_c$. Beyond V_c , we observe an inhomogeneous low moment antiferromagnetic metal, and at even larger bias a current saturated paramagnetic metal. We suggest an approximate scheme for the spectral features of this nonequilibrium system.

Keywords: Mott breakdown, Hubbard model, nonlinear transport

I. INTRODUCTION

The field driven breakdown of band insulators is a well understood phenomenon, owing to the early work of Zener¹. In these insulators electron correlation effects are neglected and the breakdown is understood in terms of field assisted quantum tunneling of electrons across the band gap. In contrast, Mott insulators are strongly correlated, with a charge gap of many body origin due to Coulomb repulsion between electrons. The nonequilibrium physics of Mott insulators has attracted a lot of attention in recent times with both experimental²⁻¹³ and theoretical^{14,15,18-30} studies trying to explore the effect of the strong electron correlation on nonlinear transport in these insulators.

Experiments have probed Mott insulators out of equilibrium by either applying a dc bias²⁻⁷, by photoexcitation¹³, or using a pulse source⁸⁻¹¹, and measured both ultrafast as well as long time (steady state) response. In most of the experiments the current voltage (I-V) characteristic at low temperature has a sharp threshold voltage³⁻⁸. The theory for band insulators predict that the I-V is given by the Landau-Zener (LZ) form $I \sim V e^{-V_{th}/V}$, with $V_{th} \propto \Delta^2 L/W$ where Δ is the band gap, L is the longitudinal size and W the bandwidth of the system. The observed I-V characteristics at Mott breakdown are quite different from the LZ response, and show a sharp threshold at low temperature.

The theoretical studies broadly use two approaches: field driven and bias driven. In the field driven approach a constant electric field is applied across the system, either by introducing a time dependent gauge field via Peierls coupling or by imposing a linear potential gradient. This has been used in the one dimensional Hubbard model to study the time-dependent Schrodinger equation¹⁴, and also in an application of the density matrix renormalisation group (DMRG)¹⁵. Dynamical mean field theory (DMFT)¹⁶ generalised to nonequilibrium situations¹⁷⁻²¹ has extensively used this approach. Many of these studies find that the I-V characteristics obey the LZ form. Recently, the Hartree-Fock mean field approach has also been used to study field driven problems. A discontinuous insulator to metal transition, along with a region of bistability, has been found within a homogeneous mean field study²².

For disordered systems, both hysteresis and filamentary conduction have been found within an unrestricted Hartree-Fock study²³.

In the bias driven setup the interacting ‘bulk’ is coupled to noninteracting leads across the sample. A chemical potential difference (bias) between the two leads tends to drive a current. Time dependent DMRG²⁴, nonequilibrium DMFT^{25,26}, and a 3D time dependent Gutzwiller mean field based study^{27,28} have used this setup. These methods *impose* a linear gradient across the system or construct a screening potential by hand²⁵. Despite the assumed form for the potential the Gutzwiller method obtains spatially inhomogeneous behaviour in various quantities. The current in these studies do not show the sharp voltage driven change that is observed in experiments³⁻⁸, and fit rather with the LZ form. A few bias driven calculations, however, do compute the internal field self consistently and find that the breakdown process is preceded by a spatially modulated state^{29,30}. This hints that the *spatial symmetry breaking* due to the applied bias can promote inhomogeneous states which play a crucial role in the breakdown.

To explore this aspect we used a Keldysh mean field approach to study the 2D Hubbard model, at half-filling and strong interaction, connected to metallic leads. Our main finding is on the non trivial spatial behaviour of the charge and spin density in the Mott insulator as the system heads towards breakdown. We observe that there is a weakly size dependent threshold voltage V_c , of order the gap in the zero bias Mott insulator, which defines the reference scale in the biased problem. Around $V = V_c$ the system shows crossover from exponentially small current to a high current state. The key features of this phenomenon can be captured by a bias dependent ‘penetration length’, $\xi(V)$, which becomes comparable to system size as $V \rightarrow V_c$.

We uncover the following progression as the bias is increased across the Mott insulator. In our notation AF-I and AF-M are antiferromagnetic insulator and metal, respectively, and PM-M is paramagnetic metal.

1. Pre-breakdown AF-I ($V \ll V_c$): In this window the charge and spin fields, ϕ_i and M_i , are weakly modified near the edge, from the $V = 0$ value. The deviation $\delta\phi_i$

and δM_i decay as $\sim e^{-R_i/\xi}$ into the bulk. There are exponential tails in the subgap density of states and a current $I \sim e^{-V_c/V}$.

2. Transition from AF-I to AF-M ($V \sim V_c$): The length-scale $\xi(V)$ ‘diverges’ as $V \rightarrow V_c$, and the current rapidly rises over a small voltage window. The mean local moment magnitude drops sharply. Subgap peaks develop in the density of states, which gain weight with increasing V .
3. Low moment AF-M ($V \gtrsim V_c$): This is a state with a large current, with small magnetic moments surviving close to the center of the system. It is an inhomogeneous antiferromagnetic metal.
4. Current saturation in PM-M, ($V \gg V_c$): The spectral features and the current no longer change with voltage and the moments become vanishingly small.

Apart from the current, and the spatial behaviour of charge and spin variables, we provide detailed results on the voltage dependence of the local DOS. We implement a perturbative scheme to evaluate the spectral features in the small bias regime.

II. MODEL AND METHOD

A. Model

We consider a 2D Mott insulator connected to non-interacting leads via tight-binding coupling. The leads serve two purpose: (i) the bias is introduced through a chemical potential difference between the leads, and (ii) the leads provide dissipative channels for the system to relax. The isolated Mott insulator when subjected to a field does not thermalise for a significantly long time, and instead gets trapped in a prethermalised metastable state³¹. The presence of metallic leads at the two edges allows relaxation into a nonequilibrium steady state (NESS)³².

We model the Mott insulator (“system”) by the repulsive Hubbard model defined on a square lattice, while the leads are modeled as tight-binding electron reservoirs. Each site at the left and the right edges of the Mott insulator, Fig.1, is coupled to the nearest bath site via tight-binding coupling.

$$\begin{aligned}
 \mathcal{H} &= \mathcal{H}_{sys} + \mathcal{H}_{bath} + \mathcal{H}_{coup} \\
 \mathcal{H}_{sys} &= \sum_{\langle ij \rangle, \sigma} -t_{ij} d_{i\sigma}^\dagger d_{j\sigma} + U \sum_i n_{i\uparrow} n_{i\downarrow} \\
 \mathcal{H}_{bath} &= \sum_{\langle ij \rangle, \sigma} t_\beta \left(c_{i\sigma}^\dagger c_{j\sigma}^\beta + h.c. \right) - \sum_{\beta, i, \sigma} \mu_\beta n_{i\sigma}^\beta \\
 \mathcal{H}_{coup} &= \sum_{\langle ij \rangle, \sigma} v_{ij} \left(c_{i\sigma}^{\dagger L} d_{j\sigma} + c_{i\sigma}^{\dagger R} d_{j\sigma} + h.c. \right) \quad (1)
 \end{aligned}$$

where t_s , μ and U are the nearest-neighbour hopping amplitude, chemical potential and onsite Coulomb repulsion strength, respectively, in the system. t_β and μ_β are the hopping strengths and the chemical potentials in the metallic

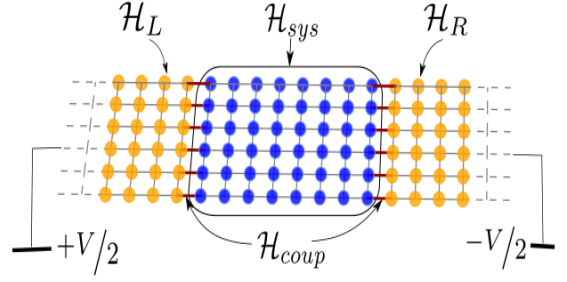


FIG. 1. Schematic diagram showing the setup. The sites having onsite Hubbard repulsion are marked in blue, while the noninteracting bath sites are marked in yellow. The coupling between the system and the bath is denoted by red bonds. The bias is applied symmetrically at the two edges by tuning the chemical potential of the baths.

baths, where $\beta = (L, R)$, with L being the left lead and R the right lead. $\mu_{L,R} = \mu \pm (V/2)$, V being the applied bias. v_{ij} denote the matrix elements of the system-bath coupling.

B. Method

1. Keldysh formulation

Assuming the leads were connected far in the past, one can write the steady-state action for the system by discretizing the complex time Keldysh contour as shown in Fig.2. The generating functional is given by:

$$Z = \int \mathcal{D}\{\bar{c}, c; \bar{d}, d\} e^{iS[\bar{c}, c; \bar{d}, d]} \quad (2)$$

where (\bar{c}, c) and (\bar{d}, d) are the Grassmann fields for the lead and system fermions respectively. $S[\bar{c}, c; \bar{d}, d]$ is the complex time Keldysh action defined on the contour.

$$\begin{aligned}
 S &= \int_{-\infty}^{\infty} dt [\mathcal{L}_{sys}(t) + \mathcal{L}_{bath}(t) + \mathcal{L}_{coup}(t)] \\
 \mathcal{L}_{sys}(t) &= \sum_{\langle ij \rangle} s \bar{d}_{i\sigma}^s(t) (i\partial_t + t_{ij}) d_{j\sigma}^s(t) - U \sum_{i, s} s n_{i\uparrow}^s n_{i\downarrow}^s
 \end{aligned}$$

FIG. 2. The complex time Keldysh contour for accessing steady states. In order to access steady states one can take t_0 (initial time) and t_{max} (maximum time) to $\pm\infty$. In order to calculate observables, e.g. the two-point function, one makes insertions at intermediate times t_1 and t_2 .

$$\begin{aligned}\mathcal{L}_{bath}(t) &= \sum_{\langle ij \rangle}^{\sigma, \alpha, s} s \bar{c}_{i\sigma\alpha}^s(t) (i\partial_t + t_{ij}^\alpha) c_{j\sigma\alpha}^s(t) \\ \mathcal{L}_{coup}(t) &= \sum_{\langle ij \rangle, \sigma, \alpha} v_{ij} \bar{c}_{i\sigma\alpha}^s(t) d_{j\sigma}(t) + h.c.\end{aligned}\quad (3)$$

where i, j are the lattice indices, σ is the spin index, α labels the leads and s labels the contour. $s = \pm 1$ for the upper and the lower contour fields respectively.

The action is quartic in the system fermion fields. To make progress we ‘decouple’ the interaction term by introducing a pair of auxiliary fields at each space-time point. We proceed as follows:

$$U n_{i\uparrow}^s n_{i\downarrow}^s = \frac{U}{4} (n_i^s)^2 - U (\mathbf{S}_i^s \cdot \hat{\Omega}_i^s)^2 \quad (4)$$

$$e^{-i\frac{sU}{4}(n_i^s(t))^2} \propto \int d\phi_i^s(t) e^{i(\frac{sU}{4}(\phi_i^s(t))^2 - \frac{sU}{2}\phi_i^s(t)n_i^s(t))} \quad (4a)$$

$$e^{isU(\mathbf{S}_i^s(t) \cdot \hat{\Omega}_i^s(t))^2} \propto \int d^3 \mathbf{M}_i^s(t) e^{i(-\frac{sU}{4}(|\mathbf{M}_i^s(t)|)^2 + sU \mathbf{M}_i^s(t) \cdot \mathbf{S}_i^s(t))} \quad (4b)$$

In the equations above, $n_i^s = \bar{c}_{i\uparrow}^s c_{i\uparrow}^s + \bar{c}_{i\downarrow}^s c_{i\downarrow}^s$ is the local density, $\mathbf{S}_i^s = \frac{1}{2} \sum_{\alpha\beta} \bar{c}_{i\alpha}^s \boldsymbol{\sigma}_{\alpha\beta} c_{i\beta}^s$ is the electron spin operator and

$\hat{\Omega}_i^s$ is an arbitrary SO(3) vector. Hubbard-Stratonovich (HS) transformation of the first term in the interaction introduces a scalar ‘‘charge field’’ $\phi_i(t)$. The HS transformation on the second term brings in an auxiliary O(3) ‘‘spin field’’ $\mathbf{M}_i(t)$.

As a result of these transformations the problem gets mapped to a quadratic Lagrangian with additional fluctuating auxiliary fields $\phi_i^\pm(t)$ and $\mathbf{M}_i^\pm(t)$. We now implement the Keldysh rotation for the fermionic and the auxiliary fields, and then integrate out the fermions (system as well as leads). The details are provided in the AppendixA. This leaves us with an action which is dependent on the ‘classical’ and ‘quantum’ auxiliary fields, which are defined as:

$$\begin{aligned}\phi_i^c(t) &\equiv \frac{1}{2}(\phi_i^+(t) + \phi_i^-(t)) \\ \phi_i^q(t) &\equiv \phi_i^+(t) - \phi_i^-(t)\end{aligned}\quad (5)$$

for the ϕ fields, and similarly for the \mathbf{M} fields.

2. Static Path Approximation (SPA)

Till this point the formulation has been exact. We have traded off the quartic interaction term for a quadratic theory with four fluctuating auxiliary fields. In order to make further progress, we introduce the static path approximation, in which we retain only the zero frequency mode of the auxiliary fields and ignore their finite frequency modes. This would be a drastic approximation if we were to consider the transient response of the system. But once the system relaxes to a NESS, one expects the average long time behaviour to be reasonably

captured by the zero frequency mode of the auxiliary fields. The effect of the finite-frequency modes can be built back perturbatively on top of the zero-mode theory, we defer that discussion to another paper. Let us introduce the notation:

$$\phi_i^{c,q}(\omega = 0) \equiv \phi_i^{c,q}, \quad \mathbf{M}_i^{c,q}(\omega = 0) \equiv \mathbf{M}_i^{c,q}$$

Under these assumptions we arrive at an effective steady state description given by the ‘static path’ action:

$$S^{SPA}[\phi, \mathbf{M}] = -iTr \ln [i\check{G}^{-1}(\omega)] + S'[\phi, \mathbf{M}] \quad (6a)$$

where,

$$\check{G}^{-1}(\omega) \equiv \begin{bmatrix} (\hat{G}^{-1}(\omega))^R & (\hat{G}^{-1}(\omega))^K \\ \hat{0} & (\hat{G}^{-1}(\omega))^A \end{bmatrix} + \hat{\Sigma} \otimes \sigma_x \quad (6b)$$

with

$$\left[(\hat{G}^{-1}(\omega))^R \right]_{ij}^{\alpha\alpha'} = \left((\omega + i\eta)\delta_{ij} + \hat{\Gamma}_{ij\alpha}^R(\omega) \right) \delta_{\alpha\alpha'} - \hat{H}_{ij}^{\alpha\alpha'} \quad (6c)$$

$$\left[(\hat{G}^{-1}(\omega))^A \right]_{ij}^{\alpha\alpha'} = \left((\omega - i\eta)\delta_{ij} + \hat{\Gamma}_{ij\alpha}^A(\omega) \right) \delta_{\alpha\alpha'} - \hat{H}_{ij}^{\alpha\alpha'} \quad (6d)$$

$$\left[(\hat{G}^{-1}(\omega))^K \right]_{ij; \alpha\alpha'} = \hat{\Gamma}_{ij\alpha}^K(\omega) \delta_{\alpha\alpha'} +$$

$$F(\omega - \mu) \left[(\hat{G}^{-1}(\omega))^R - (\hat{G}^{-1}(\omega))^A \right]_{ij}^{\alpha\alpha'} \quad (6e)$$

$$\Gamma_{ij\alpha}^{R,A,K}(\omega) = \sum_{\beta \in \{L,R\}} \left(\sum_{mn} v_{mi} v_{nj} g_{\beta, mn\alpha}^{R,A,K}(\omega) \right) \quad (6f)$$

$$\hat{H}_{ij}^{\alpha\alpha'} = -t_{\langle ij \rangle} \delta_{\alpha\alpha'} + \frac{U}{2} (\phi_i^c \delta_{\alpha\alpha'} - \mathbf{M}_i^c \cdot \boldsymbol{\sigma}_{\alpha\alpha'}) \delta_{ij} \quad (6g)$$

$$\hat{\Sigma}_{ij}^{\alpha\alpha'} = -\frac{U}{4} (\phi_i^q \delta_{\alpha\alpha'} - \mathbf{M}_i^q \cdot \boldsymbol{\sigma}_{\alpha\alpha'}) \delta_{ij} \quad (6h)$$

and

$$S'[\phi, \mathbf{M}] = \frac{U}{4\pi} \sum_i (\phi_i^c \phi_i^q - \mathbf{M}_i^c \cdot \mathbf{M}_i^q) \quad (6i)$$

$g_{\beta}^{R,A,K}(\omega)$ denote the retarded, advanced and Keldysh components of Green’s function of the reservoirs, while $\hat{G}^{R,A,K}$ denote those of the system. $\hat{\Gamma}^{R,A,K}$ is the dissipation introduced in the system due to the leads. \hat{H} is an effective Hamiltonian which one can obtain if one retains only the zero frequency mode of the auxiliary fields. $F(\omega - \mu)$ is the distribution function of the isolated system. η is a small positive number, which regulates the Keldysh action.

The mean-field consistency conditions can be obtained by extremising the SPA action with respect to the quantum auxiliary fields. We get the following family of saddle point equations:

$$\left. \frac{\delta S^{SPA}}{\delta \phi_i^q} \right|_{\phi^q, \mathbf{M}^q=0} = 0, \quad \left. \frac{\delta S^{SPA}}{\delta \mathbf{M}_i^q} \right|_{\phi^q, \mathbf{M}^q=0} = 0$$

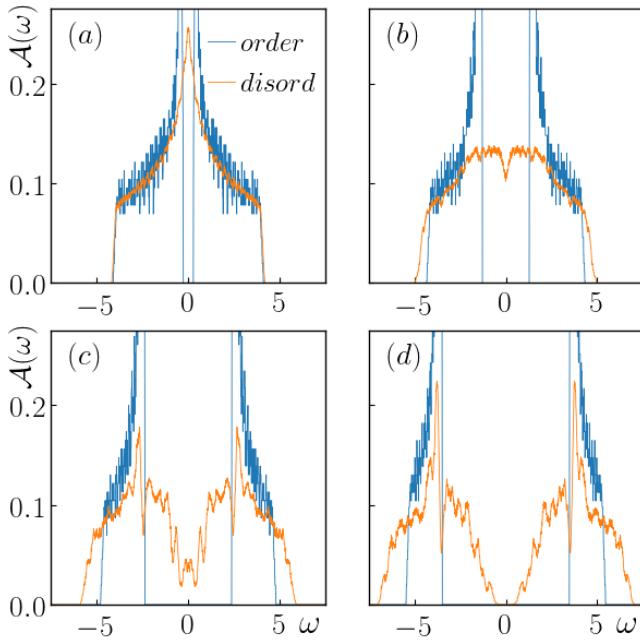


FIG. 3. (a)-(d) Comparing the density of states in the antiferromagnetic state and the ‘paramagnetic’ phase with random moment orientations for $U/t = 2, 4, 6, 8$ respectively. The ordered state remains gapped at all values of U . At $U/t = 2$, loss of order creates a gapless DOS. At $U/t = 4$, the ‘paramagnetic’ state is gapless but band singularities are absent. At $U/t = 6$ there is a pseudogap, while $U/t = 8$ shows a clean gap persisting in the ‘paramagnetic’ state.

These can be simplified to obtain the consistency conditions:

$$\int d\omega \Im \left[\text{Tr} \left(\hat{G}_{ii}^K(\omega) \right) \right] = \phi_i^c \quad (7a)$$

$$\int d\omega \Im \left[\text{Tr} \left(\hat{G}_{ii}^K(\omega) \boldsymbol{\sigma} \right) \right] = \mathbf{M}_i^c \quad (7b)$$

where $\hat{G}^K(\omega) = -\hat{G}^R(\omega) \left(\hat{G}^{-1}(\omega) \right)^K \hat{G}^A(\omega)$ and the trace is over the 2×2 spin subspace.

3. Implementation of mean field consistency

Our method involves treating the Hubbard interaction within an unrestricted Hartree-Fock (HF). We have benchmarked the scheme against the analytically tractable zero temperature mean-field limit of the equilibrium ($V = 0$) Hubbard model in 2D with periodic boundary conditions. Starting with an initial guess for $\{\phi^c \equiv \phi\}$ and $\{M_z^c \equiv M\}$, we calculate the auxiliary fields via frequency integrals of the locally projected Green’s functions. The mean field consistency equations are solved iteratively until the solutions converge for every site. The convergence criteria used is $\max_i \left[\left(\frac{\|\mathbf{M}\|_i^{n+1} - \|\mathbf{M}\|_i^n}{\|\mathbf{M}\|_i^n} \right) \leq 0.01 \right]$ or $\max_i \left[\left| \|\mathbf{M}\|_i^{n+1} - \|\mathbf{M}\|_i^n \right| < 10^{-6} \right]$, where $\|\mathbf{M}\|_i^n$ is the

magnitude of the local moment at site i in the n -th iteration. A similar criteria has used for the ϕ field as well.

In principle, one must solve for all the three components of \mathbf{M}^c at each site. For the square lattice, one can simplify the problem by retaining only the M_z^c component of the spin auxiliary field. This can be justified by performing a strong coupling expansion of the Keldysh action to find that the collinear state remains a consistent solution even at finite bias. We have elaborated on this point in Appendix B.

4. Nature of the $V = 0$ insulating state

Before launching into the voltage response we quickly discuss the nature of the $V = 0$ state. The ground state of the half filled Hubbard model on a square lattice with nearest neighbour hopping is an antiferromagnetic insulator (AF-I) for all values of U/t . However, there is a qualitative difference between the $U/t \lesssim 1$ insulator and the $U/t \gg 1$ insulator. For $U/t \lesssim 1$ one obtains a ‘Slater insulator’ where the charge gap is associated with the magnetic order. When $U/t \gg 1$, however, the charge gap (or a pseudogap) survives even when magnetic order is lost. This is the ‘Mott insulator’.

To locate the Slater to Mott crossover we used two indicators. In the first, Fig. 3, we compare the density of states (DOS) in the AF-I ground state with that in a ‘paramagnetic phase’ - where the moment magnitude is same as the AF-I state but the orientations are randomised. The results show that at $U = 6t$ the loss of magnetic order still leaves a prominent pseudogap. At this U the $V = 0$ state is a Mott insulator.

The second indicator is related to charge and spin excitation energies. The charge gap 2Δ between the upper and lower Hubbard bands at $T = 0$ crudely defines the temperature scale $T_{gap} \sim 2\Delta \sim U$ (at large U) at which the DOS would become gapless. Another scale E_{mag} arises from the energy difference between the perfect AF-I state and the random orientation state. This defines the temperature scale at which magnetic order would be lost. Fig. 4 shows that for $U/t = 6$ we are in a regime where $2\Delta \gg E_{mag}$. In fact $2\Delta \sim U$, while $E_{mag} \sim t^2/U$. Again the signature of a Mott

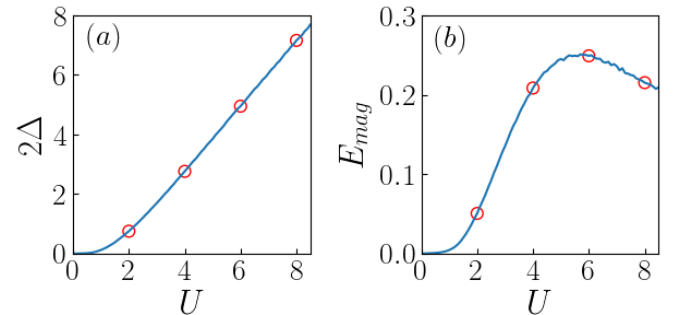


FIG. 4. (a) Charge gap 2Δ as a function of U for the Hartree-Fock ground state at equilibrium. (b) Energy difference E_{mag} between the antiferromagnetic ground state and the ‘paramagnetic’ state with random moment orientations, as a function of U . $E_{mag} \sim t^2/U$ at large U .

insulator.

A full thermal theory has indeed been developed for the equilibrium problem^{33–35} and recovers T_c scales consistent with Fig.4. See Fig.1 in³³. We are developing a non equilibrium generalisation of this approach³⁶.

III. RESULTS

We discuss the results for our implementation of the scheme in a 2D system, which is finite in the longitudinal direction, while being periodic in the transverse direction. For the tight-binding baths, we approximate the density of states by an appropriate Lorentzian function.

$$\rho_{L,R}(\omega) = \left(\frac{D}{3 \tan^{-1}(\frac{3}{2})} \right) \frac{1}{\left(\omega^2 + \left(\frac{2D}{3} \right)^2 \right)} \quad (8)$$

Where D is the bandwidth of the bath. After integrating out the bath we retain only the diagonal terms arising from the bath Green's functions, which are proportional to the bath DOS, an approximation that is justified in the wide-bandwidth limit²⁹.

Unless explicitly mentioned, we have shown the results for a system with 32 sites in the longitudinal (x) direction and 8 sites in the transverse (y) direction. We have also studied the size dependence of our results by varying the longitudinal size from 12 to 48 sites, and the transverse size from 4 to 8 sites. The size dependence has been discussed in the relevant sections. Unless otherwise mentioned, all energies are measured in units of hopping in the system t_s , and all currents are measured in units of $2et_s/\hbar$.

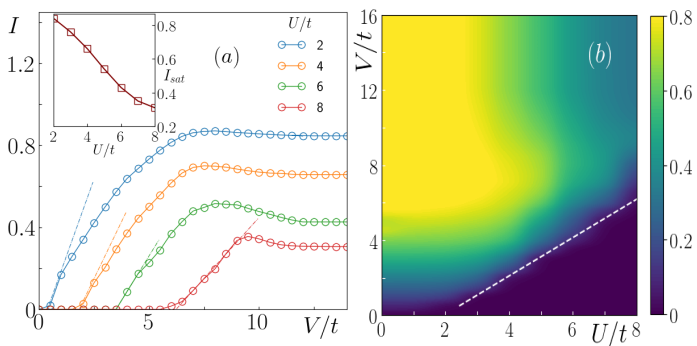


FIG. 5. (a) The $I - V$ characteristics for different values of interaction strength U , showing the transition from an insulating Mott state to a metallic state. The current rises sharply around a ‘critical bias’ V_c , and finally saturates to a scale $I_{sat}(U)$ when $V \gg V_c$. The dependence of I_{sat} on the U is shown in the inset. (b) A map of the current for varying U and V . The broken line demarcates the insulator-metal ‘phase boundary’.

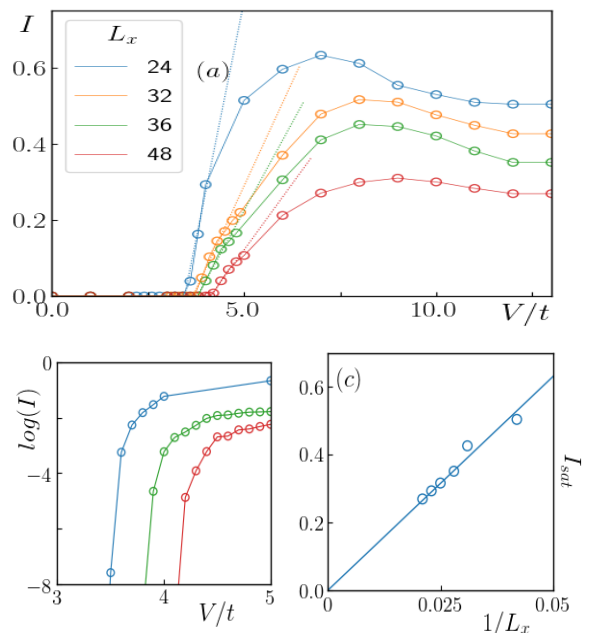


FIG. 6. (a) Size dependence of $I - V$ characteristics at $U = 6$. Both the critical bias V_c , as well as the saturation current I_{sat} depend on the longitudinal size of the system. (b) The region around V_c has been plotted in log scale to highlight its size dependence. (c) Shows the dependence of I_{sat} on the longitudinal size. The data can be fitted reasonably to $I_{sat} \propto 1/L_x$. For a fixed V the current, and the ‘metallisation’ effect in general, would vanish as $L_x \rightarrow \infty$.

A. I-V character and ‘phase diagram’

The bond current between the nearest neighbour sites in the x direction is given by the expression:

$$I_{j,j+1}(V) = \sum_{\sigma} \int_{-\infty}^{\infty} \frac{d\omega}{2\pi} (G_{j+1,j;\sigma}^<(\omega) - G_{j,j+1;\sigma}^<(\omega))$$

$$G^<(\omega) = \frac{1}{2} (G^K(\omega) + G^A(\omega) - G^R(\omega))$$

For the system in consideration, which has periodic boundary conditions along the transverse direction, the current is found to be the same along all longitudinal chains. Hence, the total current scales linearly with the transverse size of the system. At steady state one further expects the current to be the same on all bonds along the longitudinal axis. This has been numerically checked to be true strictly in the limit $\eta \rightarrow 0$.

For a sufficiently large system size and for $U \gtrsim 2$ (that we have explored given our size constraints) we find that I-V characteristic has three different regions: (i) pre-breakdown - exponentially suppressed current, (ii) breakdown - the current increases rapidly to attain its maximum value, and (iii) saturation - the current drops from the maximum to saturate at a finite value. Regime (ii) involves a transition from an AF-I to an AF-M, both spatially inhomogeneous, as we have stated earlier.

In Fig. 5(a) we plot the current (I) as a function of bias (V) for various interaction strengths U . In regime (i), when

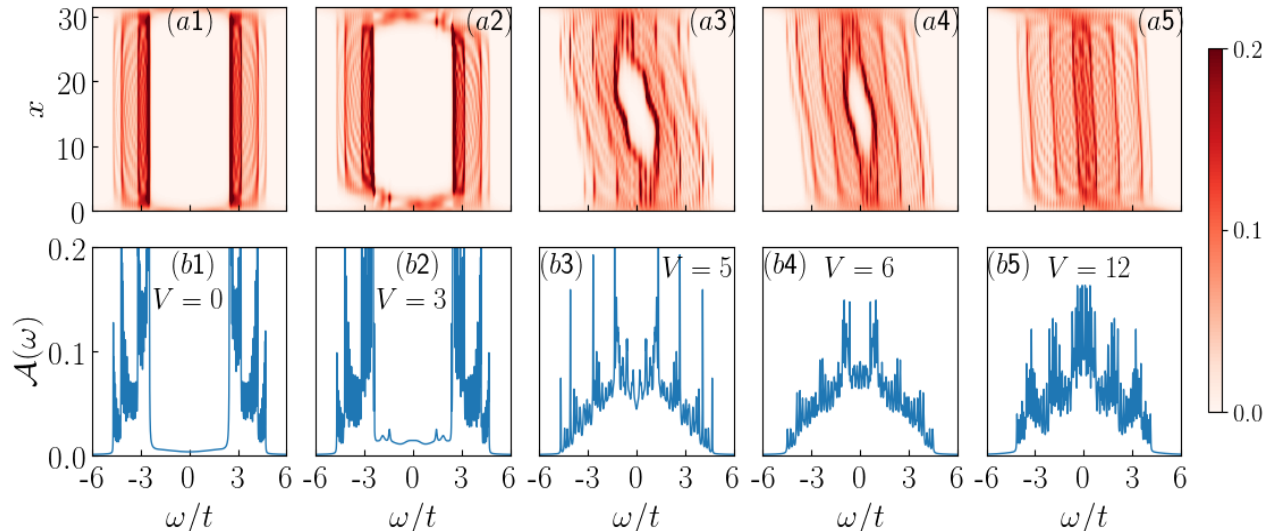


FIG. 7. Density of states: the upper row shows the variation of local DOS $A_{ii}(\omega, x)$ along the longitudinal direction, (x), with changing bias at $U = 6t$. The panels a1-a5 are for $V = \{0, 3, 5, 6, 12\}$ respectively. The regimes are (a1) the reference AF-I state at $V = 0$, (a2) AF-I at low V , (a3) AF-I to AF-M breakdown, (a4) AF-M at large current, (a5) PM-M state with current saturation. The lower row shows the behavior of the system averaged density of states with changing bias at $U = 6t$. Panels b1-b5 are for the same values of V as the respective panel above.

$V \ll V_c$, the current $I \sim e^{-V_c/V}$, Fig. 6(b), after which the system enters regime (ii), where the current increases rapidly, and then saturates in regime (iii) where $V \gg V_c$. For $U > 2$, and moderate sizes we encounter a region of negative differential resistance (NDR) in the I-V between the breakdown and saturation regimes. On studying the size dependence [Fig. 6(a)] at a fixed value of U , one finds that this effect diminishes with increasing length of the transport direction L_x , and ultimately goes away at large enough sizes. One has encountered such regions of NDR in experiments⁴.

The saturation current I_{sat} depends on the length of the system in the direction of transport L_x [Fig. 6(a)]. Being formulated in real space, our method allows us to study the size dependence of the saturation current. As shown in Fig. 6(c), $I_{sat} \sim 1/L_x$, vanishing as $L_x \rightarrow \infty$.

One can construct a ‘phase diagram’ from the current map, $I(U, V)$, in Fig. 5(b). It shows the required threshold bias as a function of U for a fixed size of the system, $V_c(U, L_x)$. Within our calculation we find $V_c(U, L_x)$ to be dependent on the longitudinal size of the system. This too has been observed in experiments⁴. The phase diagram separates the insulating regime (i) from the metallic regimes (ii) and (iii), in the $U - V$ plane. Note that for the square lattice, at half filling, the ground state becomes antiferromagnetic for an arbitrarily small U , but for $U/t \gtrsim 4$ the insulating character can survive even in the absence of magnetic order.

Within our scheme the Mott insulator supports exponentially weak current at $V < V_c(U)$ [Fig. 6(b)], but beyond $V_c(U)$ the current rises sharply and then reduces towards a saturation value. This is in contrast to the DMFT^{19,20,25} and Gutzwiller mean field²⁸ studies in which the current appears to have a functional form $I \sim V e^{-\alpha/V}$.

The $I - V$ curve in our theory has a point of inflection (second derivative vanishes) at the V_c , while the DMFT form does not have any such point. Such a point arises within our theory because the current saturates at large V , while the DMFT current keeps growing linearly at large V . Within our theory, the current saturation occurs due to the finite bandwidth of system, irrespective of the bandwidth of the bath. The behaviour we observe has similarity to some experiments^{3,7}.

B. Density of states

The density of states (DOS), $\mathcal{A}(\omega)$, is obtained by averaging the local DOS, $\mathcal{A}_{ii}(\omega)$, over the x direction.

$$\mathcal{A}_{ii}(\omega) = \sum_{\sigma} \mathcal{A}_{ii,\sigma} = -\frac{1}{\pi} \sum_{\sigma} \text{Im} (G_{ii,\sigma}^R(\omega)) \quad (9a)$$

$$\mathcal{A}(\omega) = \frac{1}{L} \sum_{i=1}^L \mathcal{A}_{ii}(\omega) \quad (9b)$$

At $V = 0$ the LDOS is gapped at all sites, except for a couple of sites at the edges - which get renormalised due to coupling with the metallic baths. The sites away from the edges remain essentially unaffected in the absence of bias, as is evident in Fig. 7(a1). The system averaged DOS, Fig. 7(b1), remains largely indistinguishable from that of an isolated system. At low bias, $V \ll V_c$, the effect of bias decays exponentially inside the system, as we will see in the next section, with a ‘penetration length’ controlled by the bias. As the penetration length increases, sites progressively away from the edges start to ‘sense’ the bias and the gap in the LDOS collapses for

these sites, Fig. 7(a2). One can now find subgap state in the DOS, even though the edges in the global DOS, Fig. 7(b2), remain sharply defined. In this regime the behaviour of the DOS can be understood, approximately, in terms of a weak site-dependent perturbation on top of a translation invariant parent state. We discuss this further in Sec.IV B.

After the breakdown, $V \gtrsim V_c$, all the sites feel the effect of the bias and a significant fraction of sites towards the edges become gapless, while the gap for sites at the center gets suppressed significantly [Fig. 7(a3)]. The overall DOS [Fig.7 (b3)] becomes gapless indicating that the fraction of ungapped sites is comparable to the gapped ones. In this regime, the gap in the LDOS shrinks with increasing V [Fig. 7(a4)], and ultimately vanishes as we hit the saturation regime [Fig. 7(a5)]. The DOS develops increasing weight around $\omega = 0$.

C. Charge and spin profiles

Within our framework the effect of the bias gets encoded in the auxiliary fields through the self-consistency. The electrons respond to the auxiliary field patterns and sense the bias through them. For the unbiased open system the charge field ϕ vanishes throughout the system, whereas the spin field magnitude is uniform (≤ 1) on all sites, except for the edge sites. We have checked that the spin field alternates from site to site even at finite V .

If the bias is applied symmetrically, i.e. $\mu_L + \mu_R = 2\mu$ condition is satisfied, then the auxiliary fields must have a specific

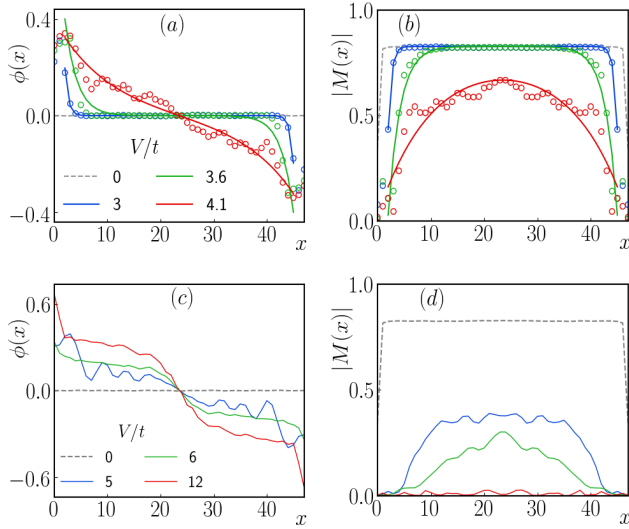


FIG. 8. Top: The auxiliary fields, $\phi(x, V)$ and $|M(x, V)|$ as a function of bias for $U = 6t$. Panels (a) and (b) show the spatial profile for a few values of V corresponding to the pre-breakdown regimes in the $I - V$ curve. The open circles denote the data points, while solid lines denote fitted curves for ϕ in (a) and $|M|$ in (b) using the trial functions. The broken lines in grey which denote the zero bias profiles for the auxiliary fields serve as the reference. Bottom: The auxiliary field profiles in the post-beakdown $V = 5, 6$ and saturation $V = 12$ regimes.

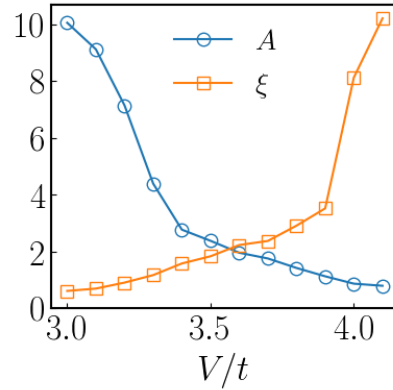


FIG. 9. The fitting parameters - penetration length ξ and scale factor A as a function of bias V , in the neighbourhood of the crossover. The results shown are for a 48×8 system at $U = 6$.

symmetry: the charge field ϕ_i is antisymmetric with respect to the center of the system, while $|\vec{M}_i|$ is symmetric. Fig.8(a) and 8(b) (open circles) show the bias dependence of the ϕ and the $|M|$ fields in the pre-breakdown regime at $U = 6t$. Till close to V_c the effect of the bias remains confined to the edges. In this regime, we obtain a ‘‘mean profile’’ for the auxiliary fields by fitting them with the trial functions:

$$\phi_{tr}(x) = A \left(e^{-x/\xi} - e^{-(L_x-x)/\xi} \right) \quad (10a)$$

$$M_{tr}(x) = \left(M_0 - A \left(e^{-x/\xi} + e^{-(L_x-x)/\xi} \right) \right) \times \cos(\pi x) \quad (10b)$$

where L_x is the length in the longitudinal direction. M_0 is the mean-field moment size for the translation invariant system. The bias dependence of the deviation fields enters through the parameters A - an overall scale factor, and ξ - the penetration length. The fitted curves for ϕ and $|M|$ have been plotted using solid lines in Fig.8(a) and 8(b).

Fig.7 shows the bias dependence of fitting parameters. For $V \ll V_c$ the effect of bias remains localised to the edges and ϕ and $|M|$ decay exponentially within a few sites from the edges. As V approaches V_c the effect of bias penetrates deeper, indicated by the rapidly rising penetration length for both the fields. Once the penetration length attains a significant value, the entire system senses the effect of bias and the current rises rapidly. Across the transition ξ grows continuously by almost an order of magnitude. The scale factor A falls rapidly before the transition and then saturates to unity beyond the transition, for all system sizes. Hence, in terms of the ‘deviation fields’ the Mott breakdown can be visualised as a transition from a strong deviation close to the edges to a system wide effect near the transition.

Beyond V_c the fields show a spatial modulation on top of a mean profile, as is evident in Fig.8(c) and 8(d). The modulations tend to die off as one approaches the saturation regime. In this regime the mean ϕ acquires a linear profile while the mean $|M|$ becomes vanishingly small. In order to analyse the

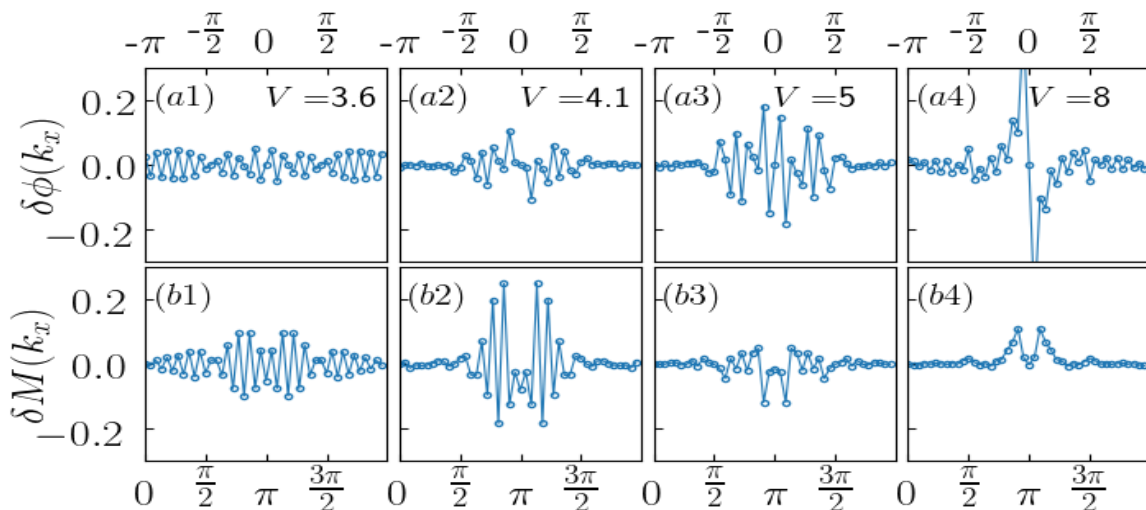


FIG. 10. Fourier content of the auxiliary field modulations at $U = 6t$ plotted for different V . The upper panels show the Fourier transform of $\delta\phi(x) = \phi(x) - \phi_{tr}(x)$, while the lower panels show the Fourier transform of $\delta M(x) = M(x) - M_{tr}(x)$. Voltages are $V = \{3.6, 4.1, 5, 8\}$ from left to right columnwise. As V increases across the transition, the interval containing the dominant modes shrinks to a narrow interval around $k_x = 0$ for $\delta\phi(k_x)$ and $k_x = \pi$ for $\delta M(k_x)$ respectively. $L_x = 48$ for the plot shown.

mode content on top of the mean profiles we subtract out the mean curve and then Fourier analyse the modulating fields $\delta\phi(x)$ and $\delta M(x)$ in the longitudinal direction, Fig.10. Before breakdown the auxiliary field profiles are dominated by the mean curves and hence, the Fourier profiles of the deviations are vanishingly small. Even for $V \lesssim V_c$, Figs. 10 (a1) and (b1), one finds that the Fourier weights are small and evenly spread over the entire k range. For $V \approx V_c$, Figs. 10 (a2),(b2) and (a3),(b3), the dominant weights lie in an interval of $\pm\frac{\pi}{2}$ around the $k = 0$ mode ϕ and $k = \pi$ mode for M . As V increases beyond V_c , the interval containing the dominant modes progressively shrinks. At $V \gg V_c$, Figs. 10 (a4) and (b4), the Fourier profile is dominated by a few modes in the vicinity of $k_x = 0$ and π for the charge and spin fields respectively. As noted in ref.²⁹, we find that spatially modulated patterns arise in the auxiliary fields as the system metallises, indicating that the system is susceptible to pattern formation. We emphasize that the transition itself is not driven by these patterns but by the suppression of the magnetic moments through the bulk of the system.

IV. DISCUSSION

In what follows we briefly touch upon the nature of the 2D transition and the large bias state, discuss an approximate method for accessing the V dependence of spectral features, and discuss some of the numerical issues related to our computation.

A. Nature of the transition and large bias state

Most experiments on the bias driven insulator-metal transition show (i) a first order jump from the insulating to the conducting state on increasing bias, (ii) a hysteretic response to bias cycling, and (iii) a seemingly growing current, an ‘ohmic response’, as the bias is increased past breakdown. We do not see these in our results at $U = 6t$ so some clarification is in order

Nature of the transition: The I-V curves for the bias driven insulator-metal transition, within this study, grow smoothly across V_c , from an exponentially suppressed current state to high current state. The transition within our *inhomogeneous* mean field study does not require the magnetic order parameter to vanish throughout the system, rather it is driven by a penetration length becoming comparable to system size - with moments still surviving in the center of the system. This is specific to low spatial dimensions - 1D and 2D, and unlike the scenario reported in Ref.²², where the system undergoes a discontinuous transition with respect to the applied field. This crucial difference might be due to the assumption of a uniform order parameter in that study. However, a 3D generalisation³⁶ of this method yields I-V characteristics in which the current switches discontinuously between the two regimes. There we also find hysteresis with respect to upward and downward voltage sweeps. This is the scenario reported in most of the experiments²⁻⁷ on voltage driven Mott insulators.

Large bias state: Within our scheme the current saturates at large values of bias since the current kernel is bounded by the bandwidth of the bath-connected system. Increasing V beyond this scale does not have any effect on the current. The range of V , post-breakdown, for which the current keeps growing depends on the ratio of gap (Δ) to the bandwidth (W). For example, in Fig.5(a), for $U/t = 2$ we have

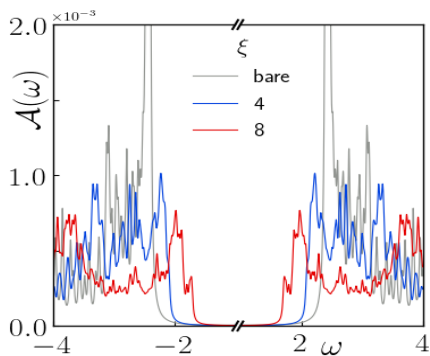


FIG. 11. The perturbatively corrected DOS, in the pre-breakdown regime for different values of ξ keeping A fixed at 1.5. The gap reduces with increasing ξ .

$\Delta/W \approx 10$, and one needs to apply a bias which is ten times larger than the breakdown voltage to find current saturation. This might be the scenario for most experiments^{2-4,6,7} where they do not report saturation upto $V \sim 2V_c$.

B. Spectrum at finite bias, $V \ll V_c$

We set up a perturbative calculation which captures the gap renormalisation in the global DOS at finite bias, $V \ll V_c$. In this regime, the deviation of the auxiliary fields from the translation invariant background profile is small, and one can treat the deviation fields $\delta\phi$ and δM within perturbation theory. In this, we neglect the contribution coming from renormalisation of the local DOS at the edges due to the hybridisation with the leads. This is justified because the edge contribution to the global DOS is suppressed by a factor of $1/L_x \ll 1$. Under these assumptions, the bare problem becomes analytically tractable. One can obtain the bare DOS by diagonalising a 2×2 Hamiltonian in momentum space. The deviation fields:

$$\delta\phi(x) = Ae^{-L/2\xi} \left(e^{(\frac{L}{2}-x)/\xi} - e^{-(\frac{L}{2}-x)/\xi} \right) \quad (11a)$$

$$\delta M(x, y) = -Ae^{-L/2\xi} \left(e^{(\frac{L}{2}-x)/\xi} + e^{-(\frac{L}{2}-x)/\xi} \right) \times \cos(\pi x + \pi y) \quad (11b)$$

are treated within perturbation theory. We compute the second order self energy corrections to the bare DOS and show, in Fig.11, that for a fixed A , the gap in the spectrum decreases with increasing ξ . The details of the calculation are provided in AppendixC.

C. Numerical checks

1. Size dependence

Our problem is formulated explicitly for a finite sized system. For a fixed V , if one takes $L_x \rightarrow \infty$ one does not expect to see a breakdown since the field inside the system vanishes.

We have studied the size dependence of the $I(V)$ character in Fig.6. The gross features in the DOS, namely the gap and the bandwidth, are less sensitive to longitudinal size variation. The fit of the auxiliary field profiles with the trial functions suggested in Eq.10(a) and 10(b) systematically improves with increasing longitudinal size. Moreover the penetration depth, ξ rises more sharply around V_c with increasing L_x . The transverse size L_y does not have any effect on the auxiliary field profiles.

2. Frequency discretisation

In order to stabilise the Schwinger-Keldysh action, even for an isolated system, one needs to work with a small, but finite η . Microscopically, this can be interpreted as slight broadening of exact eigenlevels due to weak coupling with the environment. In a numerical implementation, η should be chosen to be as small as allowed by numerical stability, and certainly smaller than the average level spacing. We find that the choice of η can affect the results significantly. The transition itself gets ‘smeared’ in this scenario. Hence, η has been chosen to be much smaller (an order of magnitude) than the average level spacing and we have ensured that reducing it further does not affect our results. The choice of η also dictates the frequency discretisation $\Delta\omega$, as one must satisfy the condition $\Delta\omega \ll \eta$ in order to satisfy the DOS sum rules. This forces us to work with a very large frequency grid $\sim 5 \times 10^3$.

V. CONCLUSION

We studied the breakdown of a two dimensional antiferromagnetic Mott insulator in response to a voltage bias, using Keldysh mean field theory at zero temperature. We obtained the current-voltage characteristics for a finite sized system and studied its size dependence. The I-V results which we obtain show a threshold behaviour, unlike those obtained from dynamical mean field theory studies. We studied the variation of the local density of states in the longitudinal direction in response to the bias. The LDOS changes from ‘gapped’ to ‘ungapped’ as one moves from the center to the edge at $V < V_c$, with the fraction of ‘ungapped’ sites increasing as one heads towards V_c . These effects emerge due to the progressive ‘penetration’ of the applied bias into the bulk over a lengthscale $\xi(V)$, which grows to system size near the critical bias. All response functions can be calculated, approximately, based on a knowledge of this lengthscale. The results emphasize the role of spatial symmetry breaking due to the applied bias, and the need for a real space treatment of the resulting problem. Our method readily generalises to disordered and frustrated Mott systems.

Acknowledgements: We acknowledge the use of HPC Clusters at HRI. AD acknowledges fruitful discussions with Abhishek Joshi and Sauri Bhattacharyya. AD would also like to thank Dibya Kanti Mukherjee and Arpita Saha for constructive criticism of the manuscript. The research of AD was supported in part by the Infosys scholarship for senior students.

Appendix A: Derivation of consistency conditions

Here we present a more detailed derivation of the consistency conditions for the static auxiliary fields. Stating from the model defined by the Hamiltonian in eq.1 one can construct the generating functional by discretizing the complex time contour as given in eq.3. Upon introducing the auxiliary fields for the upper and the lower contours at each time slice, as given in eqns. 4a and 4b, the partition function can be written as:

$$Z \propto \int \mathcal{D}\{\bar{c}, c; \bar{d}, d; \phi, M\} e^{i\tilde{S}[\bar{c}, c; \bar{d}, d; \phi, M]} \quad (\text{A1a})$$

with

$$\tilde{S} = \int_{-\infty}^{\infty} dt \left(\tilde{\mathcal{L}}_S(t) + \mathcal{L}_B(t) + \mathcal{L}_C(t) \right) \quad (\text{A1b})$$

$$\begin{aligned} \tilde{\mathcal{L}}_S(t) = & \sum_{\substack{i,j \\ \sigma,s}} s \bar{d}_{i\sigma}^s(t) (i\partial_t - \phi_i^s \delta_{ij} + t_{\langle ij \rangle} + \sigma_z M_i \delta_{ij}) d_{j\sigma}^s(t) \\ & + \frac{1}{U} \sum_{i,s} \left((\phi_i^s(t))^2 - (M_i^s(t))^2 \right) \end{aligned} \quad (\text{A1c})$$

\mathcal{L}_B and \mathcal{L}_C are the same as those defined in eq.3 and respectively. At this stage, it is convenient to perform a Keldysh rotation. The fermionic Grassmann fields are transformed as:

$$d^1 = \frac{1}{\sqrt{2}} (d^+ + d^-) \quad \bar{d}^1 = \frac{1}{\sqrt{2}} (\bar{d}^+ - \bar{d}^-) \quad (\text{A2a})$$

$$d^2 = \frac{1}{\sqrt{2}} (d^+ - d^-) \quad \bar{d}^2 = \frac{1}{\sqrt{2}} (\bar{d}^+ + \bar{d}^-) \quad (\text{A2b})$$

while the bosonic auxiliary fields transform as:

$$M^c = \frac{1}{2} (M^+ + M^-) \quad (\text{A3})$$

$$M^q = (M^+ - M^-) \quad (\text{A4})$$

where we have suppressed the time and other labels for notational brevity. A similar transformation for the ϕ field is given in eq.5. The fermions can be integrated out and the resulting action in frequency space can be written as:

$$\begin{aligned} \tilde{S}[\phi, M] = & Tr \ln (i\check{G}^{-1}(\omega, \omega')) \\ & + \frac{1}{U} \int \frac{d\omega}{2\pi} \sum_i (\phi_i^c(\omega) \phi_i^q(-\omega) - M_i^c(\omega) M_i^q(-\omega)) \end{aligned} \quad (\text{A5a})$$

where the components of \check{G}^{-1} in the 2×2 Keldysh space are

given by:

$$\begin{aligned} \left[\left(\hat{G}^{-1} \right)^R \right]_{\alpha\alpha'}^{ij} = & (\omega \delta_{ij} + t_{\langle ij \rangle} + i\hat{\Gamma}_{ij\alpha}^R(\omega)) \delta_{\alpha\alpha'} \delta(\omega - \omega') \\ & - (\phi_i^c(\omega - \omega') \delta_{\alpha\alpha'} - M_i^c(\omega - \omega') \sigma_{\alpha\alpha'}^z) \delta_{ij} \end{aligned} \quad (\text{A5b})$$

$$\begin{aligned} \left[\left(\hat{G}^{-1} \right)^{12} \right]_{\alpha\alpha'}^{ij} = & \frac{1}{2} (M_i^q(\omega - \omega') \sigma_{\alpha\alpha'}^z - \phi_i^q(\omega - \omega') \delta_{\alpha\alpha'}) \delta_{ij} \\ & + \hat{\Gamma}_{ij\alpha}^K(\omega) \delta(\omega - \omega') \delta_{\alpha\alpha'} \end{aligned} \quad (\text{A5c})$$

$$\left[\left(\hat{G}^{-1} \right)^{21} \right]_{\alpha\alpha'}^{ij} = \frac{1}{2} (M_i^q(\omega - \omega') \sigma_{\alpha\alpha'}^z - \phi_i^q(\omega - \omega') \delta_{\alpha\alpha'}) \delta_{ij} \quad (\text{A5d})$$

$$\begin{aligned} \left[\left(\hat{G}^{-1} \right)^A \right]_{\alpha\alpha'}^{ij} = & (\omega \delta_{ij} + t_{\langle ij \rangle} + i\hat{\Gamma}_{ij\alpha}^A(\omega)) \delta_{\alpha\alpha'} \delta(\omega - \omega') \\ & - (\phi_i^c(\omega - \omega') \delta_{\alpha\alpha'} - M_i^c(\omega - \omega') \sigma_{\alpha\alpha'}^z) \delta_{ij} \end{aligned} \quad (\text{A5e})$$

$\Gamma^{R,A,K}(\omega)$ are dissipation terms which enter the action as a result of integrating out the leads.

At this point one can, in principle, find the saddle point of this action with respect to the frequency dependent auxiliary fields. But for evaluating the saddle point equations one would have to invert the full frequency and site off-diagonal Green's function \mathbb{G}^{-1} . This is a very challenging task, and requires some physically motivated approximations in order to proceed. Here we invoke the static approximation, in which we drop the frequency dependence of the auxiliary fields, and thus restrict ourselves to the description of steady states only. The advantage we gain is that the Green's functions become diagonal in frequency, owing to the time-translation invariance of the NESS. This allows us to access much larger sizes, in order to establish detailed spatial dependence of various quantities of interest.

Appendix B: Justification for collinear moments

In this section we derive the form of the consistency conditions in the strong coupling limit. This allows us to cast the consistency conditions as approximate polynomial equations in terms of the auxiliary fields, with coefficients which are determined by tracing over the electrons.

We can rewrite the G^{-1} in eqn. 6b as:

$$\check{G}^{-1}(\omega) = \check{\mathcal{G}}^{-1}(\omega) + \check{\Sigma} \quad (\text{B1a})$$

with,

$$\check{\mathcal{G}}^{-1}(\omega) = \begin{bmatrix} (\omega - \hat{\Lambda}_i^c) \delta_{ij} + \hat{\Gamma}_{ij\alpha}^R(\omega) \delta_{\alpha\alpha'} & \hat{\Gamma}_{ij\alpha}^K(\omega) \delta_{\alpha\alpha'} \\ 0 & (\omega - \hat{\Lambda}_i^c) \delta_{ij} + \hat{\Gamma}_{ij}^A(\omega) \delta_{\alpha\alpha'} \end{bmatrix} \quad (\text{B1b})$$

and,

$$\check{\Sigma} = \begin{bmatrix} t_{<ij>} & \hat{\Lambda}_i^q \delta_{ij} \\ \hat{\Lambda}_i^q \delta_{ij} & t_{<ij>} \end{bmatrix} = \hat{T} \mathcal{I}^K + \hat{\Lambda}^q \sigma_1^K \quad (\text{B1c})$$

With this, we can write the SPA action given in eqn.6a in the following way:

$$S^{SPA}[\phi, \mathbf{M}] = -i \text{Tr} \ln [i \check{\mathcal{G}}^{-1}] - i \text{Tr} \ln [\mathcal{I} + \check{\mathcal{G}} \check{\Sigma}] + S' \quad (\text{B2a})$$

The first term vanishes due to the causal structure of the theory. We expand the second term in powers of Σ .

$$S^{SPA} = S^{(1)} + S^{(2)} + S^{(3)} + O(\Sigma^4) + S' \quad (\text{B2b})$$

with

$$S^{(n+1)} = i \text{Tr} \left(\left(\hat{\mathcal{G}} \hat{T} \right)^n \hat{\mathcal{G}} \hat{\Lambda}^q \sigma_1^K \right) + \dots \quad (\text{B2c})$$

The even powers of this expansion, along with the terms denoted by ellipsis vanish at the classical saddle point. We truncate the expansion to $O(t^2)$ and evaluate the classical saddle point. In this limit the saddle point equations are:

$$\left. \frac{\delta S^{SPA}}{\delta \phi_i^q} \right|_{\{q=0\}} = \frac{i}{2} \text{Tr} \left(\hat{\mathcal{G}}_i^K \right) + \frac{2}{U} \phi_i^c - \frac{it^2}{2} \sum_{z \in \text{NN}} \text{Tr} \left(\hat{\mathcal{G}}_i^K \left(\hat{\mathcal{G}}_i^R \hat{\mathcal{G}}_{i+z}^R + \hat{\mathcal{G}}_{i+z}^A \hat{\mathcal{G}}_i^A \right) + \hat{\mathcal{G}}_{i+z}^K \hat{\mathcal{G}}_i^A \hat{\mathcal{G}}_i^R \right) = 0 \quad (\text{B3a})$$

$$\left. \frac{\delta S^{SPA}}{\delta \mathbf{M}_i^q} \right|_{\{q=0\}} = -\frac{i}{2} \text{Tr} \left(\hat{\mathcal{G}}_i^K \boldsymbol{\sigma} \right) - \frac{1}{U} \mathbf{M}_i^c + \frac{it^2}{2} \sum_{z \in \text{NN}} \text{Tr} \left(\hat{\mathcal{G}}_i^K \left(\boldsymbol{\sigma} \hat{\mathcal{G}}_i^R \hat{\mathcal{G}}_{i+z}^R + \hat{\mathcal{G}}_{i+z}^A \hat{\mathcal{G}}_i^A \boldsymbol{\sigma} \right) + \hat{\mathcal{G}}_{i+z}^K \hat{\mathcal{G}}_i^A \boldsymbol{\sigma} \hat{\mathcal{G}}_i^R \right) = 0 \quad (\text{B3b})$$

where $\hat{\mathcal{G}}_i^{R,A,K}$ are the atomic Green's functions which can be expressed in terms of ϕ^c and \mathbf{M}^c . 'NN' denotes the nearest neighbours. The trace involves a matrix trace over the local spin components as well as an integral over frequency, which can be performed analytically. Hence, these constitute a complete set of equations which determine the auxiliary field profile over the entire system, as long as we stay in the regime $t^2 < U|M_i^c|$. In principle, they can be solved to obtain the ϕ , as well as the \mathbf{M} profile throughout the system.

For our purposes, it is sufficient to focus on eqn. B3b. The magnitude of the local moment is obtained by equating the

sum of first two terms to zero. Demanding that the third term should vanish determines the relative phase between neighbouring spins. After taking the trace over the spin indices and integrating over frequency, it simplifies to:

$$\left((\mathbf{M}_i \cdot \mathbf{M}_j) \mathbf{M}_i - |\mathbf{M}_i|^2 \mathbf{M}_j \right) f(\phi_i, |\mathbf{M}_i|, \phi_j, |\mathbf{M}_j|, U) = 0 \quad (\text{B4})$$

where i and j are nearest neighbour sites and $f(\phi_i, |\mathbf{M}_i|, \phi_j, |\mathbf{M}_j|, U)$ is independent of relative orientation of the moments. This can be satisfied for any value of the $\{\phi, |\mathbf{M}|\}$, provided $\left((\mathbf{M}_i \cdot \mathbf{M}_j) \mathbf{M}_i - |\mathbf{M}_i|^2 \mathbf{M}_j \right) = 0$. We can easily verify that both FM, as well as a Néel AFM state satisfies this condition. For the square lattice, we know that the Néel state is lower in energy at equilibrium, and is energetically well separated from the FM state. This serves as the justification for neglecting the M_x^c, M_y^c components of the consistency equation 7b in numerical implementation of the mean field scheme.

Appendix C: Perturbative corrections to DOS

Assume the bare Hamiltonian to be translation invariant.

$$H_0 = \sum_{\substack{\mathbf{k} \in \frac{1}{2} BZ \\ \sigma \in \pm}} \left(c_{\mathbf{k}\sigma}^\dagger \quad c_{\mathbf{k}+\mathbf{Q}\sigma}^\dagger \right) \begin{bmatrix} \epsilon_{\mathbf{k}} & \sigma M_0 \\ \sigma M_0 & -\epsilon_{\mathbf{k}} \end{bmatrix} \begin{pmatrix} c_{\mathbf{k}\sigma} \\ c_{\mathbf{k}+\mathbf{Q}\sigma} \end{pmatrix} \quad (\text{C1})$$

where $\mathbf{Q} = (\pi, \pi)$. M_0 is the moment size which can be obtained by solving the gap equation. This can be diagonalised using the transformation:

$$\begin{pmatrix} \gamma_{\mathbf{k},\sigma}^A \\ \gamma_{\mathbf{k},\sigma}^B \end{pmatrix} = \begin{pmatrix} \cos \theta_{\mathbf{k}} & \sin \theta_{\mathbf{k}} \\ \sin \theta_{\mathbf{k}} & -\cos \theta_{\mathbf{k}} \end{pmatrix} \begin{pmatrix} c_{\mathbf{k},\sigma} \\ c_{\mathbf{k}+\mathbf{Q},\sigma} \end{pmatrix} \quad (\text{C2})$$

with $\theta_{\mathbf{k}} = \tan^{-1} \left(\frac{E_{\mathbf{k}} - \epsilon_{\mathbf{k}}}{M_0} \right)$ and $E_{\mathbf{k}} = \sqrt{\epsilon_{\mathbf{k}}^2 + M_0^2}$. This maps the problem into a 2-band system separated by a gap. The retarded Green's functions for the upper and the lower bands are given by:

$$[\mathcal{G}^R(\omega)]_{\mathbf{k}}^{AA} = \text{---} \mathbf{k} \text{---} = \frac{1}{\omega - E_{\mathbf{k}} + i\eta} \quad (\text{C3})$$

$$[\mathcal{G}^R(\omega)]_{\mathbf{k}}^{BB} = \text{--} \mathbf{k} \text{--} = \frac{1}{\omega + E_{\mathbf{k}} + i\eta} \quad (\text{C4})$$

We shall suppress the label ' R ', henceforth in this section, as all the Green's functions and the self-energies shall pertain to the Retarded component. The bias acts perturbatively on the system via the charge and spin deviation fields, given in eq.11.

Implementing a discrete fourier transform on the a lattice:

$$\begin{aligned}
\delta\phi(k_x, k_y) &= \sum_{x=-L_x/2}^{L_x/2} \sum_{y=-L_y/2}^{L_y/2} e^{i(k_x x + k_y y)} \delta\phi(x) \\
&= \frac{\delta_{k_y,0}}{L_x} \int_{-L_x/2}^{L_x/2} dx e^{ik_x x} \delta\phi(x) \\
&= \frac{2A}{L_x} e^{-\frac{L_x}{2\xi} \delta_{k_y,0}} \left[\frac{\sinh\left((k_0 - ik_x) \frac{L_x}{2}\right)}{(k_0 - ik_x)} \right. \\
&\quad \left. - \frac{\sinh\left((k_0 + ik_x) \frac{L_x}{2}\right)}{(k_0 + ik_x)} \right] \quad (C5)
\end{aligned}$$

for $a_x/L_x \ll 1$, where a_x is the lattice spacing in the x-direction. Similarly,

$$\begin{aligned}
\delta M(k_x, k_y) &= -\frac{A}{L_x} e^{-\frac{L_x}{2\xi}} \left[\delta_{k_y^+,0} \left(\frac{\sinh\left((k_0 - ik_x^+) \frac{L_x}{2}\right)}{(k_0 - ik_x^+)} \right) \right. \\
&\quad \left. + \frac{\sinh\left((k_0 + ik_x^+) \frac{L_x}{2}\right)}{(k_0 + ik_x^+)} \right) + \left((k_x^+, k_y^+) \rightarrow (k_x^-, k_y^-) \right) \right] \quad (C6)
\end{aligned}$$

where $k_{x,y}^\pm = k_{x,y} \pm \pi$. The perturbation can be written in terms of the deviation fields as:

$$\begin{aligned}
H_{pert} &= \sum_{\substack{\mathbf{k}, \mathbf{q} \in \frac{1}{2}BZ \\ \sigma \in \pm}} \left(c_{\mathbf{k}\sigma}^\dagger \quad c_{\mathbf{k}+\mathbf{q}\sigma}^\dagger \right) \begin{bmatrix} \delta\phi_{\mathbf{k}-\mathbf{q}} & \sigma\delta M_{\mathbf{k}-\mathbf{q}} \\ \sigma\delta M_{\mathbf{k}-\mathbf{q}} & -\delta\phi_{\mathbf{k}-\mathbf{q}} \end{bmatrix} \begin{pmatrix} c_{\mathbf{q}\sigma} \\ c_{\mathbf{q}+\mathbf{Q}\sigma} \end{pmatrix} \\
&+ H.c. \quad (C7) \\
&= \sum_{\substack{\mathbf{k}, \mathbf{q} \in \frac{1}{2}BZ \\ \sigma \in \pm}} \left((\gamma_{\mathbf{k}\sigma}^A)^\dagger \quad (\gamma_{\mathbf{k}\sigma}^B)^\dagger \right) \begin{bmatrix} f(\mathbf{k}, \mathbf{q}) & g(\mathbf{k}, \mathbf{q}) \\ g(\mathbf{k}, \mathbf{q}) & -f(\mathbf{k}, \mathbf{q}) \end{bmatrix} \begin{pmatrix} \gamma_{\mathbf{q}\sigma} \\ \gamma_{\mathbf{q}\sigma} \end{pmatrix} \\
&+ H.c. \quad (C8)
\end{aligned}$$

where,

$$f(\mathbf{k}, \mathbf{q}) = \cos(\theta_{\mathbf{k}} + \theta_{\mathbf{q}}) \delta\phi_{\mathbf{k}-\mathbf{q}} + \sigma \sin(\theta_{\mathbf{k}} + \theta_{\mathbf{q}}) \delta M_{\mathbf{k}-\mathbf{q}} \quad (C9)$$

$$g(\mathbf{k}, \mathbf{q}) = \sin(\theta_{\mathbf{k}} + \theta_{\mathbf{q}}) \delta\phi_{\mathbf{k}-\mathbf{q}} - \sigma \cos(\theta_{\mathbf{k}} + \theta_{\mathbf{q}}) \delta M_{\mathbf{k}-\mathbf{q}} \quad (C10)$$

Self-energy: The first order self energy vanishes, since there is no $\mathbf{k} = 0$ component to the deviation fields. The second order self energy correction to the upper and lower band propagators is given by:

$$\begin{aligned}
\Sigma_{\mathbf{k}\sigma}^{AA}(\omega) &= \text{Diagram 1} + \text{Diagram 2} \\
&= \sum_{\mathbf{q} \in \frac{1}{2}BZ} \left(\frac{|f(\mathbf{k}, \mathbf{q})|^2}{\omega - E_{\mathbf{q}} + i\eta} + \frac{|g(\mathbf{k}, \mathbf{q})|^2}{\omega + E_{\mathbf{q}} + i\eta} \right) \quad (C11)
\end{aligned}$$

$$\begin{aligned}
\Sigma_{\mathbf{k}\sigma}^{BB}(\omega) &= \text{Diagram 3} + \text{Diagram 4} \\
&= \sum_{\mathbf{q} \in \frac{1}{2}BZ} \left(\frac{|f(\mathbf{k}, \mathbf{q})|^2}{\omega + E_{\mathbf{q}} + i\eta} + \frac{|g(\mathbf{k}, \mathbf{q})|^2}{\omega - E_{\mathbf{q}} + i\eta} \right) \quad (C12)
\end{aligned}$$

The corrected propagators are given by:

$$G_{\mathbf{k}\sigma}^{AA}(\omega) = \left([\mathcal{G}_{\mathbf{k}\sigma}^{AA}(\omega)]^{-1} - \Sigma_{\mathbf{k}\sigma}^{AA}(\omega) \right)^{-1} \quad (C13)$$

$$G_{\mathbf{k}\sigma}^{BB}(\omega) = \left([\mathcal{G}_{\mathbf{k}\sigma}^{BB}(\omega)]^{-1} - \Sigma_{\mathbf{k}\sigma}^{BB}(\omega) \right)^{-1} \quad (C14)$$

From this the perturbatively corrected DOS can be obtained by:

$$\mathcal{A}_{pert}(\omega) = -\frac{1}{\pi} \sum_{\mathbf{k}\sigma} \text{Im} [G_{\mathbf{k}\sigma}^{AA}(\omega) + G_{\mathbf{k}\sigma}^{BB}(\omega)] \quad (C15)$$

¹ C. Zener, Proc. R. Soc. A **145**, 523 (1934).

² I. Valmianski, P. Y. Wang, S. Wang, J. G. Ramirez, S. Guénon, and I. K. Schuller, Phys. Rev. B. **98**, 195144 (2018).

³ F. Nakamura, M. Sakaki, Y. Yamanaka, S. Tamaru, T. Suzuki and Y. Maeno, Scientific Reports **3**, 2536 (2013).

⁴ A. Zimmers, L. Aigouy, M. Mortier, A. Sharoni, S. Wang, K. G. West, J. G. Ramirez, and I. K. Schuller, Phys. Rev. Lett. **110**, 056601 (2013).

⁵ I. P. Radu, B. Govoreanu, S. Mertens, X. Shi, M. Cantoro, M. Schaeckers, M. Jurczak, S. D. Gendt, A. Stesmans, J. A. Kittl, M. Heyns and K. Martens, Nanotechnology **26** 165202.

⁶ Tai-Lung Wu, L. Whittaker, S. Banerjee, and G. Sambandamurthy, Phys. Rev. B. **83**, 073101 (2011).

⁷ R. Kumai, Y. Okimoto, and Y. Tokura, Science **284**, 1645.

⁸ F. Sabeth, T. Iimori, and N. Ohta, J. Am. Chem. Soc. 2012, **134**, 16, 6984-6986.

⁹ H. Yamakawa, T. Miyamoto, T. Morimoto, T. Terashige, H. Yada, N. Kida, M. Suda, H. M. Yamamoto, R. Kato, K. Miyagawa, K. Kanoda and H. Okamoto, Nature Materials **16**, 11001105 (2017).

¹⁰ V. Guiot, L. Cario, E. Janod, B. Corraze, V. Ta Phuoc, M. Rozenberg, P. Stoliar, T. Cren and D. Roditchev, Nature Communications **4**, 1722 (2013).

- ¹¹ C. Vaju, L. Cario, B. Corraze, E. Janod, V. Dubost, T. Cren, D. Roditchev, D. Braithwaite, and O. Chauvet, *Adv. Mater.* 2008, **20**, 27602765.
- ¹² Y. Kawasugi, H. M. Yamamoto, N. Tajima, T. Fukunaga, K. Tsukagoshi, and R. Kato, *Phys. Rev. B* **84**, 125129 (2011).
- ¹³ Y. Toda, T. Mertelj, T. Naito, and D. Mihailovic, *Phys. Rev. Lett.* **107**, 227002 (2011).
- ¹⁴ T. Oka, R. Arita, and H. Aoki, *Phys. Rev. Lett.* **91**, 066406 (2003).
- ¹⁵ T. Oka and H. Aoki, *Phys. Rev. Lett.* **95**, 137601 (2005).
- ¹⁶ A. Georges, G. Kotliar, K. Werner, and M. J. Rozenberg, *Rev. Mod. Phys.* **68**, 13 (1996).
- ¹⁷ H. Aoki, N. Tsuji, M. Eckstein, M. Kollar, T. Oka, and P. Werner, *Rev. Mod. Phys.* **86**, 779 (2014).
- ¹⁸ J. K. Freericks, V. M. Turkowski, and V. Zlatić, *Phys. Rev. Lett.* **97**, 266408 (2006).
- ¹⁹ M. Eckstein, T. Oka, and P. Werner, *Phys. Rev. Lett.* **105**, 146404 (2010).
- ²⁰ C. Aron, G. Kotliar, and C. Weber, *Phys. Rev. Lett.* **108**, 086401 (2012).
- ²¹ J. Li, C. Aron, G. Kotliar, and J. E. Han, *Phys. Rev. Lett.* **114**, 226403 (2015).
- ²² Jong E. Han, Jiajun Li, Camille Aron, and Gabriel Kotliar, *Phys. Rev. B* **98**, 035145 (2018).
- ²³ Jiajun Li, Camille Aron, Gabriel Kotliar, and Jong E. Han, *NanoLett.* 2017, 17, 5, 2994-2998.
- ²⁴ F. Heidrich-Meisner, I. González, K. A. Al-Hassanieh, A. E. Feiguin, M. J. Rozenberg, and E. Dagotto, *Phys. Rev. B* **82**, 205110 (2010).
- ²⁵ S. Okamoto, *Phys. Rev. Lett.* **101**, 116807 (2008).
- ²⁶ G. Mazza, A. Amaricci, M. Capone, and M. Fabrizio, *Phys. Rev. Lett.* **117**, 176401 (2016).
- ²⁷ M. Schiró and M. Fabrizio, *Phys. Rev. Lett.* **105**, 076401 (2010).
- ²⁸ G. Mazza, A. Amaricci, M. Capone, and M. Fabrizio, *Phys. Rev. B* **91**, 195124 (2015).
- ²⁹ P. Ribeiro, A. E. Antipov, and A. N. Rubtsov, *Phys. Rev. B* **93**, 144305 (2016).
- ³⁰ Y. Tanaka and K. Yonemitsu, *Phys. Rev. B* **83**, 085113 (2011).
- ³¹ Joura, Alexander V. and Freericks, J. K. and Lichtenstein, Alexander I., *Phys. Rev. B* **91**, 245153 (2015).
- ³² Ribeiro, P. and Vieira, V. R., *Phys. Rev. B* **92**, 100302(R) (2015).
- ³³ Anamitra Mukherjee, Niravkumar D. Patel, Shuai Dong, Steve Johnston, Adriana Moreo, and Elbio Dagotto *Phys. Rev. B* **90**, 205133 (2015).
- ³⁴ Nyayabanta Swain, Rajarshi Tiwari, and Pinaki Majumdar *Phys. Rev. B* **94**, 155119 (2016).
- ³⁵ Nyayabanta Swain, Pinaki Majumdar *J. Phys.: Condens. Matter* **29**, 085603 (2017).
- ³⁶ A. Dutta and P. Majumdar (in preparation).